The Cryosphere Discuss., 8, 1407–1451, 2014
www.the-cryosphere-discuss.net/8/1407/2014/
doi:10.5194/tcd-8-1407-2014

The Cryosphere Discussions
Open Access

Study of a temperature gradient metamorphism of snow from 3-D images: time evolution of microstructures, physical properties and their associated anisotropy

N. Calonne[1,2,3], F. Flin[1], C. Geindreau[2,3], B. Lesaffre[1], and S. Rolland du Roscoat[2,3]

[1]Météo-France – CNRS, CNRM-GAME UMR 3589, CEN, 38400 Saint Martin d'Hères, France
[2]Univ. Grenoble Alpes, 3SR, 38000 Grenoble, France
[3]CNRS, 3SR, 38000 Grenoble, France

Received: 28 January 2014 – Accepted: 30 January 2014 – Published: 28 February 2014

Correspondence to: N. Calonne (neige.calonne@meteo.fr), F. Flin (frederic.flin@meteo.fr)

Published by Copernicus Publications on behalf of the European Geosciences Union.

Abstract

We carried out a study to monitor the time evolution of microstructural and physical properties of snow during a temperature gradient metamorphism: a snow slab was subjected to a constant temperature gradient along the vertical during three weeks in a cold-room, and regularly sampled in order to obtain a set of 3-D images using X-ray microtomography. A large panel of properties was then computed from this series of 3-D images: density, specific surface area, correlation length, mean and Gaussian curvature distributions, air and ice tortuosities, effective thermal conductivity, and intrinsic permeability. Whenever possible, a specific attention was paid to assess these properties along the vertical and horizontal directions, and an anisotropy coefficient defined as the ratio of the vertical over the horizontal values was deduced. The time evolution of these properties, as well as their anisotropy coefficients, was investigated, showing the development of a strong anisotropic behavior during the experiment. Most of the computed physical properties of snow were then compared with two analytical models (*Self consistent estimates* and *Dilutes bed of spheroids*) based on the snow density, and the size and anisotropy of the grains through the correlation lengths. These models, which require only basic microstructural information, offer rather good estimates of the properties and anisotropy coefficients for our experiment without any fitting parameters. Our results highlight the interplay between the microstructure and physical properties, showing that the physical properties of snow subjected to a temperature gradient cannot be described accurately using only isotropic parameters such as the density and require more refined information. Furthermore, this study constitutes a detailed database on the evolution of snow properties under a temperature gradient, which can be used as a guideline and a validation tool for snow metamorphism models at the micro or macro scale.

TCD
8, 1407–1451, 2014

1 Introduction

Natural snowpacks are frequently subjected to temperature gradients induced by their close environment. The morphology of the snow structure at the micro scale, or microstructure, evolves with time in a typical way which is called Temperature Gradient (TG) metamorphism and wherein one of the main features is the reorganization of ice along the gradient direction by sublimation (resp. condensation) of ice (resp. water vapor) together with water vapor diffusion in the pore spaces (Yosida et al., 1955; Colbeck, 1983; Flin and Brzoska, 2008). In terms of snow type, this leads to facetted crystals and depth hoar, which constitute often the weakest layers of the snowpack. Experimental and theoretical studies such as those of Yosida et al. (1955); Akitaya (1974); Marbouty (1980); Colbeck (1983) and Satyawali et al. (2008) provide a good base of knowledge on the TG metamorphism, with descriptions of the evolution of the snow grains mostly based on photographs. With the development of X-ray microtomography for snow (Brzoska et al., 1999a; Coléou et al., 2001; Lundy et al., 2002; Pinzer and Schneebeli, 2009; Chen and Baker, 2010), very precise studies related to TG metamorphism are now available (Schneebeli and Sokratov, 2004; Kaempfer et al., 2005; Flin and Brzoska, 2008; Srivastava et al., 2010; Pinzer et al., 2012). They allow a better understanding of the mechanisms involved and highlight the impact of snow microstructure on its physical and mechanical properties.

In particular, snow properties are often expressed as functions of snow density such as for the effective thermal conductivity (Yen, 1981; Sturm et al., 1997; Calonne et al., 2011) or the permeability (Shimizu, 1970; Jordan et al., 1999; Zermatten et al., 2011; Calonne et al., 2012), leading to simple parameterizations that can be used to estimate properties in snowpack models, e.g. Crocus (Brun et al., 1989) and Snowpack (Lehning et al., 1999). However, Marbouty (1980); Schneebeli and Sokratov (2004) and Satyawali et al. (2008) have shown that during TG metamorphism, the effective thermal conductivity of snow evolves without significant changes in density, but only because of the ice/pores reorganization. Such studies suggest that there is a need to refine the

TCD
8, 1407–1451, 2014

parameterizations of snow properties, at least for snow subjected to temperature gradients. In addition, as recently shown for the effective thermal conductivity (Calonne et al., 2011; Shertzer and Adams, 2011; Löwe et al., 2013; Riche and Schneebeli, 2013) or the intrinsic permeability (Calonne et al., 2012), this type of snow exhibits specific anisotropic behaviors, and require more systematic investigations.

We propose to address these issues by studying the evolution of snow morphology together with several physical properties during a typical experiment of TG metamorphism. The main objective consists in better understanding the relationships between the snow microstructure and its properties. In this context, our paper focuses on the description of the time evolution of a snow slab of 294 $\mathrm{kg\,m^{-3}}$ subjected to a vertical temperature gradient of 43 $\mathrm{K\,m^{-1}}$ in a cold room at −4 °C. The temperature and gradient values were chosen to observe a significant but not extreme evolution of the snow in a reasonable time (three weeks of experiment). Moreover, these experimental conditions are in the range of conditions frequently undergone by natural alpine snowpacks. Snow cores were regularly sampled into the snow slab and scanned by X-ray microtomography to obtain a set of 3-D images showing the time evolution of the snow microstructure. Then, computations were performed on the 3-D images to estimate various geometrical and physical properties. Whenever possible, a specific attention was paid to assess these properties in the x, y, and z directions, z being along the direction of gravity and of the macroscopic temperature gradient. In addition, following the approach of Löwe et al. (2013), we present two anisotropic analytical models for the prediction of the physical properties of snow based on the knowledge of basic microstructural information (porosity, correlation lengths in the x, y, and z directions). This offers interesting outlooks for the improvement of the parametrizations of snow properties.

The new contributions of this study lie in the following points: (i) a wide range of snow properties (mean and Gaussian curvature distributions, directional correlation lengths, specific surface area, air and ice tortuosities, intrinsic permeability, effective thermal conductivity) are investigated during the same experiment; (ii) the time evolution of

TCD
8, 1407–1451, 2014

most of these properties is provided, allowing to monitor the anisotropy of each quantity with time; and (iii) the physical properties computed on 3-D images are compared with those predicted by anisotropic analytical models based on basic microstructural properties.

2 Materials and methods

2.1 Experimental setup and 3-D images

Natural snow was collected at Chamrousse (1800 m, French Alps) on 22 February 2011 and stored at −20 °C for two weeks. This snow was then sieved in a cold room at −5 °C to obtain a horizontal snow slab of 100 cm × 50 cm × 14 cm composed of rounded grains (RG, Fierz et al., 2009) at 300 ± 15 kg m^{-3} (result from macroscopic density measurements). The snow slab was confined at the base and the top between two copper plates whose temperature was controlled by a thermo-regulated fluid circulation. The whole system was insulated by 8 cm thick polystyrene plates. An illustration of the experimental set-up is given in Fig. 1. Isothermal conditions at −5 °C were firstly applied to the snow slab during 24 h. This aimed at sintering snow grains whose bonds may have been destroyed by sieving. During the following three weeks, the temperature of the cold room was held at −4 °C and the upper and lower copper plates were maintained at −1 °C and −7 °C, respectively, generating a steady vertical temperature gradient of 43 K m^{-1} through the snow slab.

The snow slab was sampled using a cylindrical core drill approximately every three days over the three weeks, leading to seven samples in total at the end of the experiment. Macro photographs of snow particles were also taken to characterize snow type. During the sampling operation, the temperature of the cold room was temporarily held at −7 °C (temperature of the upper copper plate) in order to minimize the change of boundary conditions of the snow slab. The polystyrene plates and the upper copper plate were punctually removed in order to access the snow slab. The samples were

TCD
8, 1407–1451, 2014

taken in the middle height of the layer and at a minimum distance of 5 cm from edges and from regions already sampled. The air gap created by the sampling was systematically refilled with freshly sieved snow to prevent strong modifications of the thermal field of the snow slab. Immediately after sampling, each snow sample was put in a plastic box and impregnated with 1-chloronaphthalene. This organic product, in liquid state above −15 °C, was poured along the box walls, filling slowly the open porosities of snow. Then, the sample was frozen in an iso-octane bath cooled by dry ice (−78 °C) to allow the solidification of the 1-chloronaphthalene. The impregnation is required to stop the metamorphism of the snow microstructure and consolidate the snow sample for the further machining process. The absorption properties of the ice, air and 1-chloronaphthalene insure a correct contrast between these three components for the X-ray tomographic acquisition. Cylindrical snow cores were extracted from the samples by machining with a drill mounted on a lathe operating in a cold room at −30 °C. Each snow core was then stuck on the upper part of a copper sample holder by a droplet of 1-chloronaphthalene and sealed into a Plexiglas cap. The prepared samples were finally stored at −20 °C until the tomographic acquisitions.

Each core was scanned using the conical X-ray microtomograph of the 3S-R lab set with an acceleration voltage of 75 kV and a current intensity of 100 µA. As this microtomograph operates in an ambient temperature room, the snow core was placed in a specially designed cryogenic cell composed of a Peltier module, allowing to maintain a regulated temperature of around −30 °C at the bottom part of the copper sample holder. A continuous dry and cold air circulation between the sample holder and the double-wall Plexiglas chambers of the cell prevents the condensation of water vapor on their sides. In addition, the heat generated by the Peltier module is dissipated by a water circulation. The whole system is able to rotate of 360° during the acquisition. Each tomographic acquisition lasted around 2 h during which 1200 radiographies were taken. Horizontal cross sections of the sample were reconstructed from radiographies using the DigiXCT[1] software. After image processing (see Flin et al., 2003; Lesaffre

[1] DigiXCT: http://www.digisens3d.com/en/soft/3-DigiXCT.html.

TCD
8, 1407–1451, 2014

et al., 2004; Hagenmuller et al., 2013), we finally obtained seven 3-D images showing the microstructural evolution of the snow slab with time. The 3-D images have a resolution of 8.4 or 9.7 µm pixel^{-1} and a volume size of 5.9^3, 9.2^3 or 9.7^3 mm^3. Detailed information for each image is given in Table 1.

2.2 Computation of structural properties

2.2.1 Density

Snow porosity ϕ (dimensionless), also called volume fraction of air, was estimated from 3-D images using a standard voxel counting algorithm. Snow density ρ_s (in kg m^{-3}) was simply deduced from ϕ such as $\rho_s = \rho_i (1 - \phi)$ where ρ_i is the ice density equal to 917 kg m^{-3}.

2.2.2 Specific surface area

The specific surface area in the x, y and z directions, noted SSA_x, SSA_y and SSA_z (in m^2 kg^{-1}), were estimated from 3-D images using a stereologic method (Arakawa et al., 2009; Flin et al., 2011) such as:

$$SSA_x = \frac{2N_x}{L\rho_s}, \quad SSA_y = \frac{2N_y}{L\rho_s}, \quad \text{and} \quad SSA_z = \frac{2N_z}{L\rho_s} \tag{1}$$

where N_x, N_y, and N_z are the total number of intersections between air and ice along parallel testing lines in the x, y, and z directions, respectively, through the entire volume, L is the total length of the testing lines (in m). We recall that the z direction corresponds to the direction of the gravity and of the macroscopic temperature gradient. In the following, we use the vector $\boldsymbol{SSA} = (SSA_x, SSA_y, SSA_z)$, where SSA_z is called the vertical component while the average value of SSA_x and SSA_y, noted SSA_{xy}, is called the horizontal component.

TCD
8, 1407–1451, 2014

2.2.3 Two-point probability function and correlation lengths

At a given time, within 3-D images of snow, we can define the following characteristic function of the air phase a:

$$I^{\mathrm{a}}(\boldsymbol{x}) = \begin{cases} 1 & \text{if } \boldsymbol{x} \text{ lies in the air phase} \\ 0 & \text{if } \boldsymbol{x} \text{ lies in the ice phase} \end{cases}$$

where $\boldsymbol{x}$ is a position vector within the sample. The one- and two-point probability functions for the air phase are then defined as:

$$S_1 = \langle I^{\mathrm{a}}(\boldsymbol{x}) \rangle \quad (2)$$

$$S_2(\boldsymbol{r}) = \langle I^{\mathrm{a}}(\boldsymbol{x}) I^{\mathrm{a}}(\boldsymbol{x}+\boldsymbol{r}) \rangle \quad (3)$$

where $\boldsymbol{r}$ is a vector and the angular brackets denote the volume average. The two-point probability function is also called the two-point correlation function or the autocorrelation function in the literature. For statistically homogeneous media, S_1 is simply equal to the porosity (ϕ) and S_2 depends on $\boldsymbol{r}$. In general, S_2 has the following asymptotic properties (Torquato, 2002):

$$S_2(\boldsymbol{r}=0) = S_1 = \phi \quad (4)$$

$$\lim_{r \to \infty} S_2(\boldsymbol{r}) = \phi^2 \quad (5)$$

Dashed lines in Fig. 2 show the two-point probability function of a snow volume after 500 h of metamorphism (referred as 7G in Table 1) computed along the x, y and z directions in blue, green and red, respectively. As proposed by Löwe et al. (2011, 2013), by fitting the $S_2(\boldsymbol{r})$ function along the coordinate axes $\beta = (x, y, z)$ to an exponential $S_2(r_\beta) = (\phi - \phi^2)\ \exp(-r_\beta / l_{\mathrm{c}_\beta}) + \phi^2$ (solid lines in Fig. 2), one obtains the correlation lengths l_{c_β} (in µm) in the x, y, and z directions noted l_{c_x}, l_{c_y} and l_{c_z} (called the vertical component), respectively. The average value of l_{c_x} and l_{c_y} is called the horizontal

TCD
8, 1407–1451, 2014

component and noted $l_{c_{xy}}$. The vector $\boldsymbol{l}_c = (l_{c_x}, l_{c_y}, l_{c_z})$ is often used to characterize the typical sizes of the heterogeneities in the microstructure, i.e. to define the characteristic lengths of an ice grain and a pore.

2.2.4 Mean and Gaussian curvatures

At a given point of a 3-D object, the surface is characterized by two principal curvatures κ_1 and κ_2, which correspond to the maximum and minimum values of curvature at this point. Negative, zero and positive values of κ_1 and κ_2 define concave, flat and convex surfaces of ice, respectively. The mean curvature C (in m^{-1}) and Gaussian curvature G (in m^{-2}) are defined as:

$$C = \frac{\kappa_1 + \kappa_2}{2} \tag{6}$$

$$K = \kappa_1 \kappa_2 \tag{7}$$

The signs of the mean and Gaussian curvatures characterize the surface shape. For the mean curvature, negative, zero and positive values correspond to concave, flat and convex surfaces of ice, respectively. For the Gaussian curvature, negative, zero and positive values represent saddle-shaped surfaces corresponding for snow to necks and connections between ice grains, flat or cylindrical surfaces, and dome-shaped surfaces (convex or concave), respectively. Note that the curvature value is inversely proportional to the typical size of the considered structure.

Many techniques have been proposed to estimate mean and Gaussian curvatures on either triangular or digital surfaces (Brzoska et al., 1999b; Nishikawa et al., 2001; Rieger et al., 2002; Zhang et al., 2002; Ogawa et al., 2006; Pottmann et al., 2009, e.g.). Curvature estimations usually imply specific accuracy issues since these estimators are particularly sensitive to noise and digitization effects. This is mainly due to the fact that curvatures are second order estimates obtained on a discrete grid. In our approach, the mean (C) and Gaussian (G) curvatures are adaptively computed from

TCD
8, 1407–1451, 2014

the largest relevant neighborhoods, limiting thus their digitization noise (see Flin et al., 2004; Brzoska et al., 2007; Wang et al., 2012 for details).

In short, we use a variational approach for C and G (Sethian, 1999) where the mean curvature can be defined as the divergence of the normal vector field $\boldsymbol{n}(p)$ at point p:

$$C(p) = \frac{\boldsymbol{\nabla} \cdot \boldsymbol{n}(p)}{2} \tag{8}$$

and the Gaussian curvature, as in the following partial differential equation:

$$G(p) = \frac{M(p)}{N(p)} \tag{9}$$

with

$$\begin{aligned} M(p) = & d_{,x}^2 (d_{,yy} d_{,zz} - d_{,yz}^2) \\ & + d_{,y}^2 (d_{,xx} d_{,zz} - d_{,xz}^2) \\ & + d_{,z}^2 (d_{,xx} d_{,yy} - d_{,xy}^2) \\ & + 2 d_{,x} d_{,y} (d_{,xz} d_{,yz} - d_{,xy} d_{,zz}) \\ & + 2 d_{,y} d_{,z} (d_{,xy} d_{,xz} - d_{,yz} d_{,xx}) \\ & + 2 d_{,x} d_{,z} (d_{,xy} d_{,yz} - d_{,xz} d_{,yy}) \end{aligned} \tag{10}$$

and

$$N(p) = (d_{,x}^2 + d_{,y}^2 + d_{,z}^2)^2 \tag{11}$$

where d is the signed distance map at p and $d_{,x}$, $d_{,y}$ and $d_{,z}$ denote the partial derivatives of d along the x, y and z coordinates, respectively. For C (Eq. 8), the normal vector field $\boldsymbol{n}(p)$ could also have been expressed as a partial derivative on d. However, we use a specific normal vector estimation as proposed by Flin et al. (2005). Such an

TCD
8, 1407–1451, 2014

approach is based on an adaptive computation of the normal vector field using volumetric information obtained from the signed distance map. This gives us a precise estimation of C while decreasing the sensitivity of this formula to digitization effects (see Flin et al., 2004). For G, we simply use Eqs. (9)–(11) where derivatives are computed on local neighborhoods whose size is obtained by the adaptive analysis computed for C (Wang et al., 2012).

2.3 Computations of tortuosity, effective thermal conductivity and permeability tensors

The full 3-D tensors of tortuosity $\boldsymbol{\tau}$ (dimensionless), of effective thermal conductivity $\mathbf{k}$ (in $\mathrm{W\,m^{-1}\,K^{-1}}$) and of intrinsic permeability $\mathbf{K}$ (in $\mathrm{m^2}$) were computed from 3-D images. For that purpose, specific boundary value problems arising from the homogenization process (Auriault et al., 2009) have been numerically solved on Representative Elementary Volumes (REVs) extracted from 3-D images of snow by using the software Geodict[2], based on a finite volume method (Thoemen et al., 2008). We define the REV of size l by Ω wherein Ω_i and Ω_a are the domains occupied by the ice and the air, respectively, and where Γ denotes the common boundary.

To compute the effective thermal conductivity tensor $\mathbf{k}$, the following boundary value problem was solved (Calonne et al., 2011):

$$\boldsymbol{\nabla}\cdot(k_\mathrm{i}(\boldsymbol{\nabla}\,\boldsymbol{t}_\mathrm{i}+\mathbf{I}))=\mathbf{0} \quad \text{within} \quad \Omega_\mathrm{i} \tag{12}$$

$$\boldsymbol{\nabla}\cdot(k_\mathrm{a}(\boldsymbol{\nabla}\,\boldsymbol{t}_\mathrm{a}+\mathbf{I}))=\mathbf{0} \quad \text{within} \quad \Omega_\mathrm{a} \tag{13}$$

$$\boldsymbol{t}_\mathrm{i}-\boldsymbol{t}_\mathrm{a}=\mathbf{0} \quad \text{on} \quad \Gamma \tag{14}$$

$$(k_\mathrm{a}(\boldsymbol{\nabla}\,\boldsymbol{t}_\mathrm{a}+\mathbf{I})-k_\mathrm{i}(\boldsymbol{\nabla}\,\boldsymbol{t}_\mathrm{i}+\mathbf{I}))\cdot\boldsymbol{n}=\mathbf{0} \quad \text{on} \quad \Gamma \tag{15}$$

$$\frac{1}{|\Omega|}\int_\Omega(\boldsymbol{t}_\mathrm{a}+\boldsymbol{t}_\mathrm{i})\mathrm{d}\Omega=\mathbf{0} \tag{16}$$

[2]Geodict: http://www.geodict.de

TCD
8, 1407–1451, 2014

where $\mathbf{I}$ is the identity tensor, $k_a = 0.024\,\mathrm{W\,m^{-1}\,K^{-1}}$ and $k_i = 2.107\,\mathrm{W\,m^{-1}\,K^{-1}}$ stand for the thermal conductivity of air and ice at 271 K respectively, and the two periodic vectors $\boldsymbol{t}_i$ and $\boldsymbol{t}_a$ are unknown. The effective thermal conductivity tensor $\mathbf{k}$ is defined as:

$$\mathbf{k} = \frac{1}{|\Omega|}\left(\int_{\Omega_a} k_a(\nabla \boldsymbol{t}_a + \mathbf{I})\mathrm{d}\Omega + \int_{\Omega_i} k_i(\nabla \boldsymbol{t}_i + \mathbf{I})\mathrm{d}\Omega\right) \quad (17)$$

The tortuosity tensor of the air phase $\boldsymbol{\tau}_a$ (resp. of the ice phase $\boldsymbol{\tau}_i$) is obtained by solving the same boundary value problem assuming that $k_a = 1$ and $k_i = 0$ (resp. $k_a = 0$ and $k_i = 1$). These tensors are defined as:

$$\boldsymbol{\tau}_a = \frac{1}{|\Omega_a|}\int_{\Omega_a}(\nabla \boldsymbol{t}_a + \mathbf{I})\mathrm{d}\Omega \quad \boldsymbol{\tau}_i = \frac{1}{|\Omega_i|}\int_{\Omega_i}(\nabla \boldsymbol{t}_i + \mathbf{I})\mathrm{d}\Omega \quad (18)$$

Let us remark that the air tortuosity is simply linked to the effective diffusion tensor for the water vapor by $\mathbf{D} = \phi D_m \boldsymbol{\tau}_a$, where D_m is the molecular diffusion coefficient (in $\mathrm{m^2\,s^{-1}}$) at the pore scale. If we assume that the porous medium is constituted of an equivalent tortuous capillary of total length l', in contrast with the REV length l, it can be shown that, by definition, $0 < \tau_a \propto (l/l')^2 < 1$. Consequently, τ_a (or τ_i) tends toward 0 or 1 when the air (or ice) structure is strongly tortuous or straight, respectively. The tortuosity is also often defined as $\tau_f \propto (l'/l)$ (Kaempfer et al., 2005) such as our tortuosity definition corresponds to the inverse of τ_f^2.

The tensor $\mathbf{K}$ of intrinsic permeability was obtained by solving the following boundary value problem:

$$\mu\Delta \boldsymbol{v} - \nabla\tilde{p} - \nabla p = \mathbf{0} \quad \text{within} \quad \Omega_a \quad (19)$$

$$\nabla \cdot \boldsymbol{v} = 0 \quad \text{within} \quad \Omega_a \quad (20)$$

$$\boldsymbol{v} = \mathbf{0} \quad \text{on} \quad \Gamma \quad (21)$$

TCD
8, 1407–1451, 2014

where the fluid velocity $\boldsymbol{v}$ and the pressure fluctuation $\tilde{p}$ (with $\langle\tilde{p}\rangle = 0$) are the periodic unknowns for a given macroscopic gradient of pressure $\boldsymbol{\nabla} p$ and where μ is the dynamic viscosity of air (in Pa s). It can be shown that $\boldsymbol{v} = -(1/\mu)\mathbf{b}\boldsymbol{\nabla} p$ where $\mathbf{b}$ is a second order tensor (Auriault et al., 2009) and consequently, the permeability tensor is defined as:

$$\mathbf{K} = \frac{1}{|\Omega|}\int_{\Omega_a} \mathbf{b}\mathrm{d}\Omega \tag{22}$$

As the non-diagonal terms of the tensors $\boldsymbol{\tau}_i$, $\boldsymbol{\tau}_a$, $\mathbf{k}$ and $\mathbf{K}$ are negligible compared to the diagonal terms (the x, y and z axes of 3-D images correspond to the principal directions of the microstructure, z being along the direction of the gravity and of the temperature gradient), we only focus on the latter ones. In the following, we note $\star_z$, $\star_{xy}$ and $\star$ as the vertical component, the average of the two horizontal components ($\star_x$ and $\star_y$), and the average of the three components of any tensor $\star = (\boldsymbol{\tau}_i, \boldsymbol{\tau}_a, \mathbf{k}$ or $\mathbf{K})$ respectively. Moreover, for the sake of simplicity, $\star_{xy}$ and $\star$ are called the horizontal and the average components, respectively.

2.4 Computations of anisotropy coefficients

The anisotropy coefficient $\mathcal{A}(\star)$ was computed for each of the microstructural and physical properties mentioned above, except for density and curvatures. This coefficient is defined as the ratio between the vertical component over the horizontal one, such as $\mathcal{A}(\star) = \star_z/\star_{xy}$ where $\star = (1/\boldsymbol{SSA}, \boldsymbol{I}_c, \boldsymbol{\tau}_i, \boldsymbol{\tau}_a, \mathbf{k}$ or $\mathbf{K})$. Thus, when the coefficient $\mathcal{A}(\star)$ is close to 1, it is considered as isotropic, and when $\mathcal{A}(\star) > 1$ (resp. < 1), the property is anisotropic and larger along the vertical (resp. horizontal) direction. Note that, since SSA_{xy} and SSA_z characterize the vertical (resp. horizontal) surfaces, we study the anisotropy coefficient of the inverse of the specific surface area $1/\boldsymbol{SSA} = (1/\mathrm{SSA}_x, 1/\mathrm{SSA}_y, 1/\mathrm{SSA}_z)$ to be consistent with the other coefficients.

TCD
8, 1407–1451, 2014

2.5 Re-adjustment in density

After sieving, the density of the snow slab exhibited slight spatial inhomogeneities ($300 \pm 15\,\mathrm{kg\,m^{-3}}$, from macroscopic measurements with a corer). In order to focus only on the evolution of snow properties driven by the temperature gradient, readjusted values of effective thermal conductivity and permeability, k^{r} and K^{r}, were computed as if the density was homogeneous in the snow slab and equal to $294\,\mathrm{kg\,m^{-3}}$ (average of the density values computed from 3-D images) using the regression proposed in Calonne et al. (2011) and Calonne et al. (2012), respectively, as follows:

$$k^{\mathrm{r}} = \frac{k \times k^{\mathrm{fit}}(\rho_{\mathrm{s}})}{k^{\mathrm{fit}}(\rho_{294})} \tag{23}$$

$$K^{\mathrm{r}} = \frac{K \times K^{\mathrm{fit}}(\rho_{\mathrm{s}})}{K^{\mathrm{fit}}(\rho_{294})} \tag{24}$$

with ρ_{s} the computed snow density, $\rho_{294} = 294\,\mathrm{kg\,m^{-3}}$, $k^{\mathrm{fit}}(\rho_{\mathrm{s}}) = 2.5 \times 10^{-6}\rho_{\mathrm{s}}^2 - 1.23 \times 10^{-4}\rho_{\mathrm{s}} + 0.024$ and $K^{\mathrm{fit}}(\rho_{\mathrm{s}}) = 3.0 \times r_{\mathrm{es}}^2 \exp(-0.0130 \times \rho_{\mathrm{s}})$ where the equivalent sphere radius $r_{\mathrm{es}} = 3/(\mathrm{SSA} \times \rho_{\mathrm{i}})$. By this way, we obtained readjusted values at a density of $294\,\mathrm{kg\,m^{-3}}$ of thermal conductivity (k_x^{r}, k_y^{r}, k_z^{r}) and of permeability (K_x^{r}, K_y^{r}, K_z^{r}).

2.6 Analytical models based on ellipsoidal inclusions

We consider two analytical models based on ellipsoidal inclusions allowing to estimate the physical properties of snow including their anisotropy: the self consistent estimates and the dilute beds of ellipsoids. These models require basic microstructural information obtained from 3-D images, which are the volume fraction of each phase (ϕ, $1-\phi$) and the inclusion characteristics (size and anisotropy) given by the correlation lengths ($l_{c_x}, l_{c_y}, l_{c_z}$).

TCD
8, 1407–1451, 2014

2.6.1 Self consistent estimates: effective thermal conductivity and air tortuosity

According to the self consistent method (Bruggeman, 1935; Hill, 1965; Budiansky, 1965; Willis, 1977; Torquato, 2002), the snow microstructure is considered as a macroscopically anisotropic composite of two different types of aligned isotropic ellipsoidal inclusions of the same shape, such as the semiaxes are defined as $a = (l_{c_x} + l_{c_y})/4$ and $b = l_{c_z}/2$, with volume fractions ϕ, $1-\phi$ and conductivities k_a, k_i (see Fig. 3). Each type of inclusion is embedded in an homogeneous equivalent medium, i.e. an infinite matrix whose effective thermal conductivity $\mathbf{k}^{sc}$ is the unknown to be calculated. The solution of equations for an isolated inclusion then gives an implicit relation which can be solved for this effective property (Eq. 25). For simple inclusion shapes, this method often yields algebraic expressions of the effective properties. This self consistent scheme treats each phase symmetrically: Eq. (25) is invariant under the simultaneous interchange $k_a \leftrightarrow k_i$ and $\phi \leftrightarrow 1-\phi$. This particular property can be viewed as a way to capture the connectivity of both phases. By contrast, in the so called generalized self consistent method or three phase model (Hashin, 1962; Christensen and Lo, 1979; Boutin, 2000; Boutin and Geindreau, 2010), bi-composite inclusions are considered, typically a spherical particle (phase 1) surrounded by a concentric shell (phase 2), which allows to capture that the matrix (phase 2) and dispersed particles (phase 1) are connected and disconnected, respectively.

In the present case, the standard self consistent estimate of the effective thermal conductivity $\mathbf{k}^{sc}$ verifies (Torquato, 2002):

$$\phi(k_a\mathbf{I}-\mathbf{k}^{sc})\left(\mathbf{I}+\mathbf{A}\mathbf{k}^{sc-1}(k_a\mathbf{I}-\mathbf{k}^{sc})\right)^{-1}+(1-\phi)(k_i\mathbf{I}-\mathbf{k}^{sc})\left(\mathbf{I}+\mathbf{A}\mathbf{k}^{sc-1}(k_i\mathbf{I}-\mathbf{k}^{sc})\right)^{-1}=0 \quad (25)$$

where $\mathbf{A}$ is the depolarization tensor for an ellipsoid in a matrix with an effective thermal conductivity $\mathbf{k}^{sc}$ and is defined in the (x, y, z) frame as:

$$\mathbf{A}=\begin{pmatrix} Q & 0 & 0 \\ 0 & Q & 0 \\ 0 & 0 & 1-2Q \end{pmatrix} \quad (26)$$

TCD
8, 1407–1451, 2014

where

$$Q = \frac{1}{2}\left(1 + \frac{1}{(b/a)^2 - 1}\left(1 - \frac{1}{2\chi_b}\ln\left(\frac{1+\chi_b}{1-\chi_b}\right)\right)\right) \quad \text{if} \quad b/a \geq 1 \tag{27}$$

$$Q = \frac{1}{2}\left(1 + \frac{1}{(b/a)^2 - 1}\left(1 - \frac{1}{\chi_a}\tan^{-1}\left(\frac{1+\chi_b}{1-\chi_b}\right)\right)\right) \quad \text{if} \quad b/a \leq 1 \tag{28}$$

with $\chi_a^2 = -\chi_b^2 = (a/b)^2 - 1$. Let us remark that, for spheres, $b/a = 1$ and $Q = 1/3$; thus the tensor $\mathbf{A} = \mathbf{I}/3$ and the tensor $\mathbf{k}^{sc}$ is isotropic. In general, the inclusion shape implies that the tensor $\mathbf{k}^{sc}$ is transverse isotropic. Thus, from Eqs. (25) and (26), the horizontal components of $\mathbf{k}^{sc}$ are written:

$$k_x^{sc} = k_y^{sc} = \frac{-(k_a(\phi - Q) + k_i((1-\phi) - Q)) - \sqrt{\Delta}}{2(Q-1)} \tag{29}$$

where $\Delta = (k_a(\phi - Q) + k_i((1-\phi) - Q))^2 - 4(Q-1)Qk_ik_a$. The vertical component k_z^{sc} is obtained by replacing Q by $(1 - 2Q)$ in Eq. (29).

The self consistent estimate of the air tortuosity tensor $\boldsymbol{\tau}_a^{sc}$ can be easily deduced from (29), and we have:

$$\boldsymbol{\tau}_a^{sc} = \phi^{-1}\mathbf{k}^{sc}(k_a = 1, k_i = 0) \tag{30}$$

Figure 3 depicts the evolution of $k_x^{sc} = k_y^{sc}$ and k_z^{sc} vs. the ice volume fraction for $b/a = 1.45$ i.e. $Q = 0.38$. On this figure, the two-point bounds for anisotropic composites (Willis, 1977) are also reported. The corresponding microstructure of the lower bounds (resp. upper bounds) can be viewed as ellipsoidal inclusions of ice (resp. air) of same aspect ratio (b/a) dispersed within the air matrix (resp. ice matrix), as shown by the upper part of Fig. 3. As expected, in each direction, the self consistent estimate lies between the bounds. At low volume fractions of ice (resp. at high volume fractions),

TCD
8, 1407–1451, 2014

the self consistent estimates and the lower bounds (resp. the upper bounds) are very close. Finally, Fig. 3 clearly shows the anisotropy of the effective thermal conductivity induced by the anisotropy of the microstructure. In this particular case, $\mathcal{A}(\mathbf{k}^{sc})$ ranges from 1 to 2.8 in the whole range of ice volume fraction.

2.6.2 Dilute beds of spheroids: permeability

In that case, the snow is seen as a dilute dispersion of ellipsoids of ice in a matrix of air. As previously, the semiaxes of each ellipsoid are still defined as: $a = (l_{c_x} + l_{c_y})/4$ and $b = l_{c_z}/2$. It can be shown (Torquato, 2002) that the permeability tensor estimate $\mathbf{K}^{el}$ is written in the (x, y, z) frame:

$$\mathbf{K}^{el} = \frac{2a^2}{9(1-\phi)} \begin{pmatrix} f(b/a) & 0 & 0 \\ 0 & f(b/a) & 0 \\ 0 & 0 & g(b/a) \end{pmatrix} \tag{31}$$

where

$$f(b/a) = \frac{3}{16\chi_b^3}\left((3\chi_b^2 - 1)\ln\left(\frac{1+\chi_b}{1-\chi_b}\right) + 2\chi_b\right) \quad \text{if} \quad b/a \geq 1 \tag{32}$$

$$f(b/a) = \frac{3}{8\chi_a^3}\left((1+3\chi_a^2)\tan^{-1}(\chi_a) - \chi_a\right) \quad \text{if} \quad b/a \leq 1 \tag{33}$$

and with

$$g(b/a) = \frac{3}{8\chi_b^3}\left((1+\chi_b^2)\ln\left(\frac{1+\chi_b}{1-\chi_b}\right) - 2\chi_b\right) \quad \text{if} \quad b/a \geq 1 \tag{34}$$

$$g(b/a) = \frac{3}{4\chi_a^3}\left((\chi_a^2 - 1)\tan^{-1}(\chi_a) + \chi_a\right) \quad \text{if} \quad b/a \leq 1 \tag{35}$$

TCD
8, 1407–1451, 2014

By definition, this estimation of the permeability does not depend on the spatial arrangement of the ellipsoids, and consequently does not capture the real tortuosity of the porous media induced by the connectivity of both air and ice phases. In order to overcome this problem, the following estimation of the permeability tensor $\mathbf{K}^{di}$ is proposed:

$$\mathbf{K}^{di} = \boldsymbol{\tau}_a^{sc}\mathbf{K}^{el} \tag{36}$$

This relation allows to recover a classical expression of the permeability as $K^{di} \propto h(\phi)\tau_a d_c^2 = h(\phi)d_c^2/\tau_f^2$, where h is a function of the porosity and d_c is a characteristic length of the microstructure.

3 Results

3.1 Time evolution of microstructural and physical properties of snow

Figure 4 illustrates the time evolution of the snow microstructure during the experiment of temperature gradient metamorphism. 3-D images obtained from X-ray tomography are presented together with the corresponding vertical cross-section and photograph. The color coding of the 3-D images corresponds to the mean curvature field. For a better visualization of the facetted shapes, the images are presented "upside down": the top (respectively, base) of the images corresponds to the lowest (highest) and warmest (coolest) side of the physical sample. We observe qualitatively that the initial rounded grains become bigger and bigger and more angular and facetted with time. After about 200 h, depth hoar is obtained showing characteristic striations on the surface of grains (see photographs in Fig. 4). At the end of the experiment, the ice structure is preferably arranged along the vertical direction, i.e. the direction of the temperature gradient, as shown by the cross-sections in particular.

All the snow properties computed on the 3-D images are summarized in Table 1. The time evolution of snow density, specific surface area, correlation length, tortuosity

TCD
8, 1407–1451, 2014

of ice and air, thermal conductivity and permeability are depicted in Fig. 5. The blue, green and red symbols represent the x, y and z values of the considered property, respectively. One can observe that:

- The snow density shows no significant evolution with time and the average value over the experiment is 294 $\mathrm{kg\,m^{-3}}$ (porosity of 0.68). In detail, low variations between 275 and 315 $\mathrm{kg\,m^{-3}}$ are observed from one image to another (Fig. 5a). As explained in Sect 2.5, these variations reflect the spatial heterogeneity initially present in the sieved snow layer, and not a real time evolution generated by the temperature gradient conditions.
- The average values in the three directions of specific surface area decrease continuously with time from 27.7 to 13.4 $\mathrm{m^2\,kg^{-1}}$. Between 0 and 144 h, the z values are slightly higher than the horizontal ones (29.2 against 26.9 $\mathrm{m^2\,kg^{-1}}$ at 0 h). After 144 h, values in the three directions become very close from each other (Fig. 5b).
- The values of correlation length increase continuously during the experiment, evolving from 71 to 181 µm in the xy directions and from 68 to 228 µm in the z direction (Fig. 5c).
- The values of air tortuosity (~ 0.7) are around five times higher than those of ice tortuosity (~ 0.15) (Fig. 5d). The overall evolution of both properties is low and can be divided in two stages: the ice (resp. air) tortuosity decreases (resp. increases) between 0 and 73 h and then slightly increases (resp. decreases) until the end of the experiment. During the second stage, the z values stand out and become increasingly higher than the horizontal ones for both phases.
- The raw values of the effective thermal conductivity, which are referred as "computed" and depicted by the dashed lines in Fig. 5e, exhibit the same variations as the snow density, showing the strong relationship between these two variables. The values range between 0.14 and 0.26 $\mathrm{W\,m^{-1}\,K^{-1}}$, all directions combined.

TCD
8, 1407–1451, 2014

Solid lines in Fig. 5e, referred as "readjusted", show values of thermal conductivity after readjustment at a density of 294 kg m^{-3}. As explained in Sect. 2.5, this readjustment is one way to estimate the thermal conductivity without taking into account the influence of density variations. The evolution of readjusted values is thus smoother than the one of computed values, but as much significant. Computed and readjusted values decrease from 0 to 73 h and then continuously increase until the end of the metamorphism, showing an evolution in two stages similar to the one of tortuosities. After 73 h, the z values become much higher than the xy values with time.

– The computed values of permeability range between 0.70×10^{-9} and 4.84×10^{-9}m^2, all directions combined. They exhibit an opposite evolution to the one of snow density, but this dependence seems less pronounced than for the thermal conductivity. Indeed, despite the influence of density, a significant evolution is still observed during the metamorphism (dashed lines in Fig. 5f). Both computed and readjusted values increase over the experiment and vertical values become higher than the horizontal ones after 217 h.

Figure 6 shows the time evolution of the anisotropy coefficient for six snow properties. In overall, the evolution is the same for all properties: the coefficient increases from values lower than one at the beginning of the experiment to values greater than one at the end. In detail, the magnitude of the coefficients is strongly different from one variable to another. The largest evolution is shown by the coefficient of ice tortuosity $\mathcal{A}(\boldsymbol{\tau}_\mathrm{i})$, which increases from 0.86 to 1.90 between 0 and 144 h and then slightly decreases to reach 1.70 at the end of the metamorphism. The anisotropy coefficient of the thermal conductivity $\mathcal{A}(\mathbf{k})$ increases from 0.90 to 1.34. The largest increases of $\mathcal{A}(\boldsymbol{\tau}_\mathrm{i})$ and $\mathcal{A}(\mathbf{k})$ are observed between 0 and 144 h, showing that changes are almost concentrated during this period for both of the properties, as already pointed out above with the Fig. 5. The correlation length and permeability show similar values of anisotropy coefficients, which evolve from 0.96 to 1.25 and from 0.91 to 1.23, respectively. Finally,

TCD
8, 1407–1451, 2014

anisotropy coefficients of air tortuosity and of the inverse of the specific surface area are the smallest and evolve during the experiment from 0.97 to 1.13 and from 0.92 to 1.01, respectively.

The distributions, expressed in terms of occurrence ratio, of the mean curvature of the upward (left) and downward (right) surfaces of ice are presented in Fig. 7. They give the proportion in % of the ice surface area that exhibits a mean curvature located in a particular range of values. The time evolution of these distributions is shown by the plots of different colors. Initially (red color), the distribution of upward and downward surfaces are similar, with a peak of mean curvature located around $6\,mm^{-1}$ and an occurrence ratio of $\sim 3\,\%$. With time, the peak of mean curvature moves toward lower curvature values and sharpens, meaning that ice structures tend to become larger and of monodisperse size. At the end of the experiment (purple color), the upward and downward surfaces exhibit clearly distinct distributions: the peak of mean curvature is now located at $1\,mm^{-1}$ (occurrence ratio of 4.2 %) for the upward ones, and at $0\,mm^{-1}$ (occurrence ratio of 4.8 %) for the downward ones.

Using the same representation, Fig. 8 shows the Gaussian curvature distributions computed from the entire ice–air interface. All the distributions are centered at $0\,mm^{-2}$, but become tighter over time, with maximum occurrence ratios evolving from 4.5 % to 17.3 % between 0 and 500 h, implying that the proportion of large, flat or cylindrical structures of ice increases. The initial distribution (red color) stands out from the others: it exhibits occurrence ratios which are small between around -50 and $50\,mm^{-2}$ and large between around -300 and $-50\,mm^{-2}$, compared to those of other distributions. The most important changes in Gaussian curvatures of ice surfaces appear thus early after the beginning of the temperature gradient, where high negative values corresponding to small saddle-shaped structures disappear in favor of low values close to $0\,mm^{-2}$, reflecting large and less curved structures. Qualitatively, the same observations can be done from the 3-D images of snow at 0 (left) and 500 h (right) of metamorphism represented in Fig. 9 by looking at the color maps of Gaussian curvature. In the initial image, we see a lot of green color (negative Gaussian curvature) at

TCD
8, 1407–1451, 2014

bonds between grains, while the final image exhibits mainly yellow-based colors (nearly zero Gaussian curvatures) representing flat and large structures. The seven images of snow represented with the color map of the Gaussian curvature, as well as those of the mean curvature, are available in the auxiliary materials.

3.2 Comparisons with analytical models

Figure 10 shows the comparison between the time evolution of computed values (dashed lines) and values given by analytical models (solid lines) of air tortuosity, effective thermal conductivity and permeability. Computed values are given in the x, y and z directions while the ones given by models are described in the z and xy directions (the vertical and the horizontal plane). In order to quantitatively compare models with experiments, we use in the following $E_\star$, the mean of relative differences, defined as

$$E_\star = \frac{\star_{\text{from model}} - \star_{\text{computed}}}{\star_{\text{computed}}}, \tag{37}$$

where $\star$ is a component or the anisotropy coefficient of $\boldsymbol{\tau}_a$, $\mathbf{k}$ and $\mathbf{K}$. $E_\star$ is given with the associated standard deviation. For the vertical values of properties, $E_{\tau_{a_z}} = 6.9 \pm 5.4\,\%$, $E_{k_z} = -13.4 \pm 13.2\,\%$ and $E_{K_z} = -9.1 \pm 11.7\,\%$, whereas for the horizontal ones, $E_{\tau_{a_{xy}}} = 7.7 \pm 4.7\,\%$, $E_{k_{xy}} = -19.4 \pm 9.0\,\%$ and $E_{K_{xy}} = -8.5 \pm 14.1\,\%$.

Using the same representation, the time evolution of anisotropy coefficients from computed values and values given by models of the three above properties is shown in Fig. 11. For the air tortuosity, permeability and thermal conductivity, $E_{\mathcal{A}(\boldsymbol{\tau}_a)} = -0.7 \pm 0.9\,\%$, $E_{\mathcal{A}(\mathbf{K})} = -0.3 \pm 2.9\,\%$ and $E_{\mathcal{A}(\mathbf{k})} = 9.9 \pm 27.9\,\%$, respectively.

TCD
8, 1407–1451, 2014

4 Discussion

4.1 Evolution of the microstructure

From the mean curvature distributions (Fig. 7) and the 3-D images (Fig. 4), we observe that the snow microstructure undergoes a strong directional faceting under temperature gradient. At the beginning of the experiment, the top and base of ice grains are identical in shape and exhibit mainly convex surfaces, characteristic of rounded grains. With time, these regions become strongly different, showing mostly convex surfaces at the top and facetted surfaces at the bottom of the grains, which is typical of facetted crystals and depth hoar. This asymmetric behavior can be attributed to the growth (resp. decay) properties of the ice crystal at the molecular level, where some sites are energetically more stable for the condensation (resp. sublimation) of a water molecule (see TLK or Kossel crystal models in Markov, 1995; Mutaftschiev, 2001). Thus, the convex surfaces that are submitted to condensation undergo a layer by layer growth process resulting in the production of facets. Conversely, the sublimation of convex crystals preferentially leads to the generation of kink and step sites, which results in the rounding of the shapes (see e.g. Knight, 1966; Flin and Brzoska, 2008, for more details). Our mean curvature results confirm the above considerations: during our metamorphism experiment, the top (resp. base) of the ice structures is warmer (resp. colder) than the surrounding air and sublimates (resp. condenses), inducing a rounding (resp. facetting) of the surface due to the crystalline properties of ice.

From the temporal evolution of the snow (e.g. Fig. 5), the metamorphism can be divided in two periods: (i) between 0 and 73 h, the microstructure, resulting from equi-temperature conditions, recrystallizes toward a new pattern of structure to adapt to the temperature gradient conditions. In particular, the small but numerous connections between grains sublimate in favor to the growth of large structures (see Gaussian curvature distributions in Fig. 8). During this transitional state, the ice structure become more tortuous (minimum value of tortuosity over the whole experiment reached at 73 h in Fig. 5d), because of the decrease of the links between grains. (ii) After 73 h, the

TCD
8, 1407–1451, 2014

structure evolves in the continuity of the pattern developed during the first stage (consolidation): grains and connections become increasingly larger especially in the gradient direction, and the ice network becomes gradually less tortuous.

Because the air tortuosity is about five times higher than the ice tortuosity (see Fig. 5d), our snow samples can be considered as constituted by a tortuous skeleton of ice surrounded by large channels of air in the three directions. Our initial z value of ice tortuosity of 0.19 (referred as 0A in Table 1) is quantitatively in good agreement with the work of Kaempfer et al. (2005) who computed from a 3-D image of rounded grains at 268 kg m^{-3} a vertical ice tortuosity of $\tau_f^2 = 4.4$, which corresponds to 0.23 according to our tortuosity definition. In accordance with the observations of Schneebeli and Sokratov (2004) and Satyawali et al. (2008), the snow density remains constant over the experiment, while grains and pores grow continuously as shown by correlation lengths and curvature distributions. It means that the microstructure is re-built without a supply or loss of mass. Moreover, the snow becomes more and more anisotropic with a structure elongated in the vertical direction, as illustrated by the anisotropy coefficients of the correlation length and of the ice tortuosity. From a thermodynamic point of view, this microstructural anisotropy can be seen as a way to decrease the vertical temperature gradient by enhancing the heat flow in that direction (Staron et al., 2014).

4.2 Link with the physical properties

Heat conduction in snow is mostly due to the conduction of ice which conduces 100 times more than the air. Consequently, the effective thermal conductivity of snow is strongly linked to its density (ice proportion) and to the ice tortuosity (way for heat conduction), as illustrated in Fig. 5. Anisotropy of thermal conductivity is lower than that of ice tortuosity because the air phase taken into account in the computation of conduction reduces this anisotropy. Air conduction cannot be neglected in the computations of snow effective conductivity even if the ratio k_i / k_a is about 88 at 271 K, as already shown by Calonne et al. (2011).

TCD
8, 1407–1451, 2014

We observe two distinct stages in the evolution of the effective thermal conductivity (Fig. 5e): a decrease between 0 and 73 h, followed by an increase until the end of the experiment. This observation is in agreement with the result of Schneebeli and Sokratov (2004) who also noticed a two-stage evolution of this property (snow and temperature conditions were however different to that of our experiment). This behavior can be related to the evolution of the microstructure explained in Sect. 4.1, since (i) the destruction of connections between grains during the first period of temperature gradient limits the heat conduction in snow and (ii) the growth of large ice structures in a second time, in particular in the z direction, enhances the heat transfer.

As already mentioned, the intrinsic permeability is proportional to $h(\phi)\tau_a d_c^2$, where d_c is a characteristic length of the microstructure which could be linked to the correlation length or to the inverse of the specific surface area (Calonne et al., 2011). Consequently, the anisotropy of the permeability depends on both anisotropies of the air tortuosity and of the chosen characteristic length. Since the anisotropy coefficient of permeability, air tortuosity, and correlation length present similar time evolutions, while that of the inverse of the specific surface area stands out by remaining close to one (see Fig. 6), our results seem to show that the anisotropy of the permeability is mainly related to that of the air tortuosity and the correlation length. The fact that the permeability is related to the density and a characteristic length can explain that this property is less influenced by the density variations than the thermal conductivity as described in Sect. 3.1, but undergoes the same continuous increase over the experiment that is observed for the characteristic length.

Figure 5 shows an overall increase of the effective thermal conductivity and permeability at a constant density, underlying the role of the microstructure rearrangement (Schneebeli and Sokratov, 2004; Satyawali et al., 2008). Moreover, a significant vertical anisotropy is observed for both variables with coefficients until ~ 1.3. Thus, for snow subjected to a temperature gradient, the first approximation of expressing the physical properties depending on the density and on a single characteristic length for the permeability (e.g. Shimizu, 1970; Yen, 1981; Sturm et al., 1997; Calonne et al., 2011,

TCD
8, 1407–1451, 2014

2012) should be improved by introducing for instance new microstructural parameters which could reflect the anisotropy phenomena.

4.3 Modelling physical properties

The computed effective properties of snow were compared with analytical models based on basic information on microstructure such as the snow density and the anisotropy of the grain shape through the correlation lengths. Even if these models fail to reflect all the details of the microstructure (bonds between grains ...), our results clearly show that they allow to capture in overall the evolution of the considered properties with a mean of relative differences ranging from −19.4 % to 7.7 % (see Sect. 3.1). These models do not include any fitting parameter, by contrast with the model of Löwe et al. (2013), where the lower bounds equation (see Fig. 3) was adjusted to the computed data of thermal conductivity by introducing two parameters. These parameters are necessary since the lower bounds equation does not take into account the connectivity of both phases, in contrast with the self consistent estimates. In both of the presently proposed models, the time evolution of physical properties during the metamorphism mainly depends on one parameter Q which is associated to the shape heterogeneity (pore/grain). They could be improved by introducing (i) other information on the microstructure by computing three- or four-point probability functions on 3-D images (Torquato, 2002) or (ii) refined variables allowing to describe the evolution of grain shapes and contacts between grains (mean and Gaussian curvatures, fabric tensor) during the metamorphism.

5 Conclusions

An experiment of temperature gradient (TG) metamorphism was realized in cold room in order to monitor the evolution of microstructural and physical properties of snow over time: seven snow samples were collected at regular intervals of time over three

TCD
8, 1407–1451, 2014

weeks into a snow slab subjected to a vertical temperature gradient of 43 K m^{-1}. Each sample was scanned by X-ray tomography to obtain a series of 3-D images showing the microstructural evolution of the snow slab during the temperature gradient metamorphism. Numerical computations were performed on these 3-D images to estimate various geometrical and physical properties of snow, such as the directional correlation lengths, the mean and Gaussian curvatures, the specific surface area, the air and ice tortuosities, the effective thermal conductivity and the intrinsic permeability. When possible, such quantities were evaluated in the x, y and z directions to monitor the evolution of their anisotropy.

The main results concerning the TG experiment can be summarized as follows: (i) As shown by many other studies, density remained almost constant during the whole experiment. (ii) The grains were continuously facetting at their bottom parts while the upper parts underwent rounding due to ice sublimation. (iii) In overall, grain and neck growths were observed during the metamorphism. (iv) The intrinsic permeability, linked mainly to the air phase, increased continuously. (v) The snow microstructure evolved in two stages: a short period of strong modifications of the ice structure due to the TG initiation (0–73 h), where the ice tortuosity and the thermal conductivity decreased, followed by a stage of consolidation of this new structure (73–500 h), where the above properties increased gradually. (vi) The anisotropy coefficients of all properties increased during the metamorphism, with larger values in the gradient direction.

These results highlight the strong interplay between microstructure and physical properties of snow, and confirm that the density alone, or any isotropic quantity, is not sufficient to describe the time evolution of physical properties during a TG metamorphism. To solve this problem, we applied analytical anisotropic models (self consistent estimates and dilute bed of spheroids) using microstructural parameters (directional correlation lengths) that reflect the general shape of heterogeneities (size, anisotropy). The proposed analytical models, whose results were compared to those obtained by numerical computations, offer good estimates of the physical properties and anisotropy coefficients, without any fitting parameters.

TCD
8, 1407–1451, 2014

In overall, this study presents numerical tools to quantitatively monitor snow properties using 3-D images and provides a detailed database describing snow under a TG metamorphism. In particular, it provides a quantification of snow anisotropy, which is a key -but challenging- parameter to access directly with physical measurements during such a process. Used as a guideline or a validation tool, this database offers new outlooks for the development of micro and macro-scale snow models.

Supplementary material related to this article is available online at http://www.the-cryosphere-discuss.net/8/1407/2014/tcd-8-1407-2014-supplement.pdf.

Acknowledgements. Funding by Météo-France, INSU-LEFE and DigitalSnow (ANR-11-BS02-009-03) is acknowledged. We thank P. Charrier and J. Desrues of the 3S-R laboratory where the 3-D images were obtained. We are also grateful to J. Roulle, J.-M. Panel, P. Puglièse, C. Carmagnola and S. Morin of the CNRM-GAME for their support during the experiment. N. Calonne thanks S. Morin for his co-supervision of her Master internship during which the TG experiment has been realized. CNRM-GAME/CEN is part of the Labex OSUG@2020 (ANR10 LABX56).

References

Akitaya, E.: Studies of depth hoar, Low. Temp. Sci. Series A, 26, 1–67, 1974. 1409

Arakawa, H., Izumi, K., Kawashima, K., and Kawamura, T.: Study on quantitative classification of seasonal snow using specific surface area and intrinsic permeability, Cold. Reg. Sci. Technol., 59, 163–168, doi:10.1016/j.coldregions.2009.07.004, 2009. 1413

Auriault, J.-L., Boutin, C., and Geindreau, C.: Homogenization of coupled phenomena in heterogenous media, Wiley-ISTE, London, 2009. 1417, 1419

Boutin, C.: Study of permeability by periodic and self consistent homogenisation, Eur. J. Mech. A-Solid., 19, 603–632, 2000. 1421

TCD
8, 1407–1451, 2014

Boutin, C. and Geindreau, C.: Periodic homogenization and consistent estimates of transport parameters through sphere and polyhedron packings in the whole porosity range, Phys. Rev. E, 82, 036313-1–036313-18, 2010. 1421

Bruggeman, D.: The calculation of various physical constants of heterogeneous substances. I. The dielectric constants and conductivities of mixtures composed of isotropic substances, Ann. Phys., 24, 636–679, 1935. 1421

Brun, E., Martin, E., Simon, V., Gendre, C., and Coléou, C.: An energy and mass model of snow cover suitable for operational avalanche forecasting, J. Glaciol., 35, 333–342, 1989. 1409

Brzoska, J.-B., Coléou, C., Lesaffre, B., Borel, S., Brissaud, O., Ludwig, W., Boller, E., and Baruchel, J.: 3D visualization of snow samples by microtomography at low temperature, ESRF Newsletter, 32, 22–23, 1999a. 1409

Brzoska, J.-B., Lesaffre, B., Coléou, C., Xu, K., and Pieritz, R. A.: Computation of 3D curvatures on a wet snow sample, Eur. Phys. J.-Appl. Phys., 7, 45–57, doi:10.1051/epjap:1999198, 1999b. 1415

Brzoska, J.-B., Flin, F., and Ogawa, N.: Using Gaussian curvature for the 3D segmentation of snow grains from microtomographic data, in: Physics and Chemistry of Ice, edited by: Kuhs, W., Special Publication Nr 311, RSC Publishing, Cambridge, UK, Proceedings of the 11th International Conference on the Physics and Chemistry of Ice held at Bremerhaven, Germany, 23–28 July 2006, 125–132, 2007. 1416

Budiansky, B.: On the elastic moduli of some heterogeneous materials, J. Mech. Phys. Solids, 13, 223–227, 1965. 1421

Calonne, N., Flin, F., Morin, S., Lesaffre, B., du Roscoat, S. R., and Geindreau, C.: Numerical and experimental investigations of the effective thermal conductivity of snow, Geophys. Res. Lett., 38, L23501, doi:10.1029/2011GL049234, 2011. 1409, 1410, 1417, 1420, 1430, 1431

Calonne, N., Geindreau, C., Flin, F., Morin, S., Lesaffre, B., Rolland du Roscoat, S., and Charrier, P.: 3-D image-based numerical computations of snow permeability: links to specific surface area, density, and microstructural anisotropy, The Cryosphere, 6, 939–951, doi:10.5194/tc-6-939-2012, 2012. 1409, 1410, 1420, 1432

Chen, S. and Baker, I.: Evolution of individual snowflakes during metamorphism, J. Geophys. Res., 115, D21114, doi:10.1029/2010JD014132, 2010. 1409

Christensen, R. M. and Lo, K. H.: Solutions for effective shear properties in three phase sphere and cylinder model, J. Mech. Phys. Solids, 27, 315–330, 1979. 1421

TCD
8, 1407–1451, 2014

Colbeck, S. C.: Ice crystal morphology and growth rates at low supersaturations and high temperatures, J. Appl. Phys., 54, 2677–2682, 1983. 1409

Coléou, C., Lesaffre, B., Brzoska, J.-B., Ludwig, W., and Boller, E.: Three-dimensional snow images by X-ray microtomography, Ann. Glaciol., 32, 75–81, doi:10.3189/172756401781819418, 2001. 1409

Fierz, C., Armstrong, R. L., Durand, Y., Etchevers, P., Greene, E., McClung, D. M., Nishimura, K., Satyawali, P. K., and Sokratov, S. A.: The international classification for seasonal snow on the ground, IHP-VII Technical Documents in Hydrology no. 83, IACS Contribution no. 1, UNESCO-IHP, Paris, France, 2009. 1411, 1440

Flin, F. and Brzoska, J.-B.: The temperature gradient metamorphism of snow: vapour diffusion model and application to tomographic images, Ann. Glaciol., 49, 17–21, doi:10.3189/172756408787814834, 2008. 1409, 1429

Flin, F., Brzoska, J.-B., Lesaffre, B., Coléou, C., and Pieritz, R. A.: Full three-dimensional modelling of curvature-dependent snow metamorphism: first results and comparison with experimental tomographic data, J. Phys. D Appl. Phys., 36, A49–A54, doi:10.1088/0022-3727/36/10A/310, 2003. 1412

Flin, F., Brzoska, J.-B., Lesaffre, B., Coléou, C., and Pieritz, R. A.: Three-dimensional geometric measurements of snow microstructural evolution under isothermal conditions, Ann. Glaciol., 38, 39–44, doi:10.3189/172756404781814942, 2004. 1416, 1417

Flin, F., Brzoska, J.-B., Coeurjolly, D., Pieritz, R. A., Lesaffre, B., Coléou, C., Lamboley, P., Teytaud, O., Vignoles, G. L., and Delesse, J.-F.: Adaptive estimation of normals and surface area for discrete 3-D objects: application to snow binary data from X-ray tomography, IEEE T. Image Process., 14, 585–596, doi:10.1109/TIP.2005.846021, 2005. 1416

Flin, F., Lesaffre, B., Dufour, A., Gillibert, L., Hasan, A., Rolland du Roscoat, S., Cabanes, S., and Pugliese, P.: On the computations of Specific Surface Area and Specific Grain Contact Area from snow 3D images, in: P. C. I., edited by: Furukawa, Y., Hokkaido University Press, Sapporo, JP, proceedings of the 12th International Conference on the Physics and Chemistry of Ice held at Sapporo, Japan, 5–10 September 2010, 321–328, 2011. 1413

Hagenmuller, P., Chambon, G., Lesaffre, B., Flin, F., and Naaim, M.: Energy-based binary segmentation of snow microtomographic images, J. Glaciol., 59, 859–873, doi:10.3189/2013JoG13J035, 2013. 1413

Hashin, Z.: The elastic moduli of heterogeneous materials, J. Appl. Mech.-T. ASME , 29, 143–150, 1962. 1421

TCD
8, 1407–1451, 2014

Hill, R.: A self consistent mechanics of composite materials, J. Mech. Phys. Solids, 13, 213–222, 1965. 1421
Jordan, R., Andreas, E., and Makshtas, A.: Heat budget of snow-covered sea ice at North Pole 4, J. Geophys. Res., 104, 7785–7806, 1999. 1409
Kaempfer, T., Schneebeli, M., and Sokratov, S.: A microstructural approach to model heat transfer in snow, Geophys. Res. Lett., 32, L21503, doi:10.1029/2005GL023873, 2005. 1409, 1418, 1430
Knight, C. A.: Formation of crystallographic etch pits on ice and its application to the study of hailstones, J. Appl. Meteorol., 5, 710–714, 1966. 1429
Lehning, M., Bartelt, P., Brown, B., Russi, T., Stöckli, U., and Zimmerli, M.: SNOWPACK model calculations for avalanche warning based upon a new network of weather and snow stations, Cold Reg. Sci. Technol., 30, 145–157, 1999. 1409
Lesaffre, B., Broska, J.-B., Coléou, C., Flin, F., and Pieritz, R.: Images tridimensionnelles de neige: des prélévements in situ aux fichiers de données volumiques. Application à une expérience de métamorphose d'isothermie, Tech. Rep., CNRM-GAME CEN, Météo France – CNRS, 2004. 1412
Löwe, H., Spiegel, J., and Schneebeli, M.: Interfacial and structural relaxations of snow under isothermal conditions, J. Glaciol., 57, 499–510, doi:10.3189/002214311796905569, 2011. 1414
Löwe, H., Riche, F., and Schneebeli, M.: A general treatment of snow microstructure exemplified by an improved relation for thermal conductivity, The Cryosphere, 7, 1473–1480, doi:10.5194/tc-7-1473-2013, 2013. 1410, 1414, 1432
Lundy, C. C., Edens, M. Q., and Brown, R. L.: Measurement of snow density and microstructure using computed tomography, J. Glaciol., 48, 312–316, doi:10.3189/172756502781831485, 2002. 1409
Marbouty, D.: An experimental study of temperature-gradient metamorphism, J. Glaciol., 26, 303–312, 1980. 1409
Markov, I. V.: Crystal growth for beginners, World Scientific Publishing Co. Pte. Ltd, Singapore, 1995. 1429
Mutaftschiev, B.: The atomistic nature of crystal growth, Series in Material Science, Springer, Berlin, 2001. 1429

TCD
8, 1407–1451, 2014

Nishikawa, Y., Koga, T., Hashimoto, T., and Jinnai, H.: Measurements of interfacial curvatures of bicontinuous structure from three-dimensional digital images. 2. A sectioning and fitting method, Langmuir, 17, 3254–3265, 2001. 1415

Ogawa, N., Flin, F., and Brzoska, J.-B.: Representation of two curvatures of surface and its application to snow physics, Memoirs of the Hokkaido Institute of Technology, 34, 81–87, 2006. 1415

Pinzer, B. and Schneebeli, M.: Breeding snow: an instrumented sample holder for simultaneous tomographic and thermal studies, Meas. Sci. Technol., 20, 095705, doi:10.1088/0957-0233/20/9/095705, 2009. 1409

Pinzer, B. R., Schneebeli, M., and Kaempfer, T. U.: Vapor flux and recrystallization during dry snow metamorphism under a steady temperature gradient as observed by time-lapse micro-tomography, The Cryosphere, 6, 1141–1155, doi:10.5194/tc-6-1141-2012, 2012. 1409

Pottmann, H., Wallner, J., Huang, Q.-X., and Yang, Y.-L.: Integral invariants for robust geometry processing, Comput. Aided Geom. D., 26, 37–60, 2009. 1415

Riche, F. and Schneebeli, M.: Thermal conductivity of snow measured by three independent methods and anisotropy considerations, The Cryosphere, 7, 217–227, doi:10.5194/tc-7-217-2013, 2013. 1410

Rieger, B., Timmermans, F. J., and van Vliet, L. J.: Estimation of curvature on surfaces in 3D grey-value images, in: Proc ASCI 2002, 8th annual conf. of the advanced school for computing and imaging, 170–177, 2002. 1415

Satyawali, P. K., Singh, A. K., Dewali, S. K., Kumar, P., and Kumar, V.: Time dependence of snow microstructure and associated effective thermal conductivity, Ann. Glaciol., 49, 43–50, 2008. 1409, 1430, 1431

Schneebeli, M. and Sokratov, S. A.: Tomography of temperature gradient metamorphism of snow and associated changes in heat conductivity, Hydrol. Process., 18, 3655–3665, doi:10.1002/hyp.5800, 2004. 1409, 1430, 1431

Sethian, J. A.: Level set methods and fast marching methods: Evolving interfaces in computational geometry, fluid mechanics, computer vision, and materials science, Vol. 3, Cambridge University Press, 1999. 1416

Shertzer, R. H. and Adams, E. E.: Anisotropic thermal conductivity model for dry snow, Cold Reg. Sci. Technol., 69, 122–128, doi:10.1016/j.coldregions.2011.09.005, 2011. 1410

Shimizu, H.: Air permeability of deposited snow, Contributions from the Institute of Low Temperature Science, A22, 1–32, 1970. 1409, 1431

TCD
8, 1407–1451, 2014

Srivastava, P., Mahajan, P., Satyawali, P., and Kumar, V.: Observation of temperature gradient metamorphism in snow by X-ray computed microtomography: measurement of microstructure parameters and simulation of linear elastic properties, Ann. Glaciol., 51, 73–82, 2010. 1409

Staron, P. J., Adams, E. E., and Miller, D. A.: Nonequilibrium thermodynamics of kinetic metamorphism in snow, Cold Reg. Sci. Technol., 97, 60–71, doi:10.1016/j.coldregions.2013.10.007, 2014. 1430

Sturm, M., Holmgren, J., König, M., and Morris, K.: The thermal conductivity of seasonal snow, J. Glaciol., 43, 26–41, 1997. 1409, 1431

Thoemen, H., Walther, T., and Wiegmann, A.: 3D simulation of macroscopic heat and mass transfer properties from the microstructure of wood fibre networks, Compos. Sci. Technol., 68, 608–616, doi:10.1016/j.compscitech.2007.10.014, 2008. 1417

Torquato, S.: Random heterogeneous materials: microstructure and macroscopic properties, Springer, 2002. 1414, 1421, 1423, 1432

Wang, X., Gillibert, L., Flin, F., and Coeurjolly, D.: Curvature-driven volumetric segmentation of binary shapes: An application to snow microstructure analysis, in: Proceedings of the 21st International Conference on Pattern Recognition, ICPR 2012, Tsukuba, Japan, 11–15 November 2012, 742–745, 2012. 1416, 1417

Willis, J. R.: Bounds and self-consistent estimates for the overall properties of anisotropic composites, J. Mech. Phys. Solids, 25, 185–202, 1977. 1421, 1422

Yen, Y. C.: Review of thermal properties of snow, ice and sea ice, Tech. Rep. 81-10, CRREL, Hanover, NH, USA, 1981. 1409, 1431

Yosida, Z., Oura, H., Kuroiwa, D., Huzioka, T., Kojima, K., Aoki, S., and Kinosita, S.: Physical studies on deposited snow: I Thermal properties, Tech. Rep. 7, Institute of Low Temperature Science, Hokkaido University, Sapporo, Japan, 1955. 1409

Zermatten, E., Haussener, S., Schneebeli, M., and Steinfeld, A.: Tomography-based determination of permeability and Dupuit–Forchheimer coefficient of characteristic snow samples, J. Glaciol., 57, 811–816, doi:10.3189/002214311798043799, 2011. 1409

Zhang, Y., Paik, J., Koschan, A., Abidi, M. A., and Gorsich, D.: Simple and efficient algorithm for part decomposition of 3-D triangulated models based on curvature analysis, in: Proceedings of the 2002 International Conference on Image Processing, vol. 3, pp. III-273–III-276, IEEE, 2002. 1415

TCD
8, 1407–1451, 2014

Table 1. Microstructural and physical properties computed from 3-D images. Snow types are given according to the international classification (Fierz et al., 2009).

Name		0A	1A	2A	3A	4A	5G	7G
Snow type		RG	RG	FC	DH	DH	DH	DH
Length size of 3-D image (mm)		5.9	5.9	5.9	5.9	5.9	9.7	9.2
Resolution of 3-D image (µm)		8.4	8.4	8.4	8.4	8.4	9.7	9.7
Time under temperature gradient (h)		0	73	144	217	313	409	500
Density ρ_s (kg m^{-3})		315	275	283	275	315	286	310
Porosity ϕ (–)		0.657	0.700	0.692	0.700	0.656	0.688	0.622
SSA (m^2 kg^{-1})	x	27.4	22.8	20.8	18.2	15.2	15.0	13.5
	y	26.5	22.6	20.5	18.2	15.2	14.8	13.4
	z	29.2	24.7	21.0	18.2	14.6	14.9	13.3
Correlation length l_c (µm)	x	70	95	104	128	146	160	181
	y	73	98	109	133	147	160	182
	z	66	91	112	143	174	202	225
Air tortuosity τ_a (–)	x	0.73	0.77	0.73	0.71	0.66	0.66	0.63
	y	0.74	0.77	0.74	0.71	0.65	0.66	0.63
	z	0.71	0.76	0.76	0.76	0.73	0.73	0.71
Ice tortuosity τ_i (–)	x	0.21	0.09	0.08	0.08	0.14	0.12	0.16
	y	0.22	0.09	0.09	0.08	0.13	0.12	0.15
	z	0.19	0.12	0.16	0.15	0.25	0.21	0.27
Thermal conductivity **k** (W m^{-1} K^{-1})	x	0.22	0.14	0.14	0.14	0.19	0.16	0.20
	y	0.23	0.14	0.14	0.14	0.18	0.17	0.19
	z	0.21	0.15	0.18	0.18	0.25	0.21	0.26
Permeability **K** ($\times 10^{-9}$ m^2)	x	0.76	1.75	1.95	2.98	2.71	3.77	3.92
	y	0.78	1.74	1.95	2.89	2.61	3.70	3.95
	z	0.70	1.64	2.02	3.08	3.18	4.39	4.84

TCD
8, 1407–1451, 2014

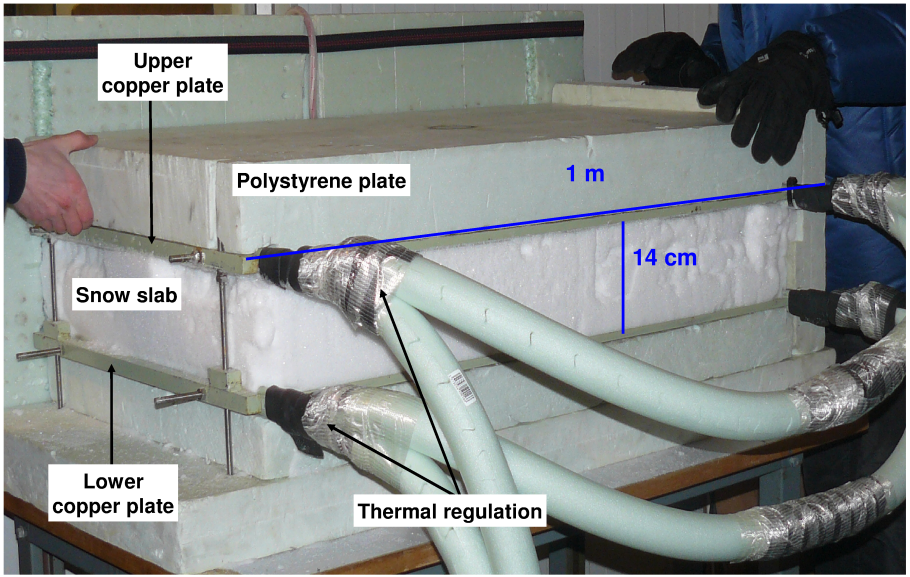

Fig. 1. Photograph in cold room of the apparatus designed to control and monitor temperatures at the top and bottom of a snow slab. The forward and left vertical polystyrene plates are here removed from the device for the visualization purposes.

TCD
8, 1407–1451, 2014

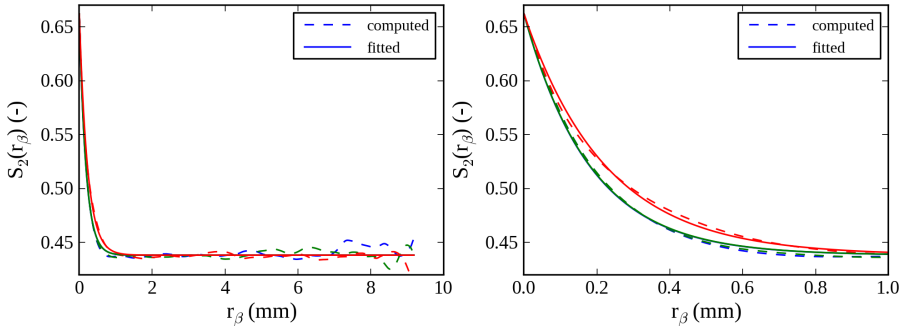

Fig. 2. Two-point probability function $S_2(\boldsymbol{r})$ for the whole range of $\boldsymbol{r}$ (left) and zoomed (right) in the x (blue), y (green) and z directions (red), obtained from the 3-D image referred as 7G in Table 1. Solid and dashed lines correspond respectively to the values computed from Eq. (3) and to the results of the expression $S_2(r_\beta) = (\phi - \phi^2)\ \exp(-r_\beta / l_{c_\beta}) + \phi^2$ with $\beta = (x, y, z)$.

TCD
8, 1407–1451, 2014

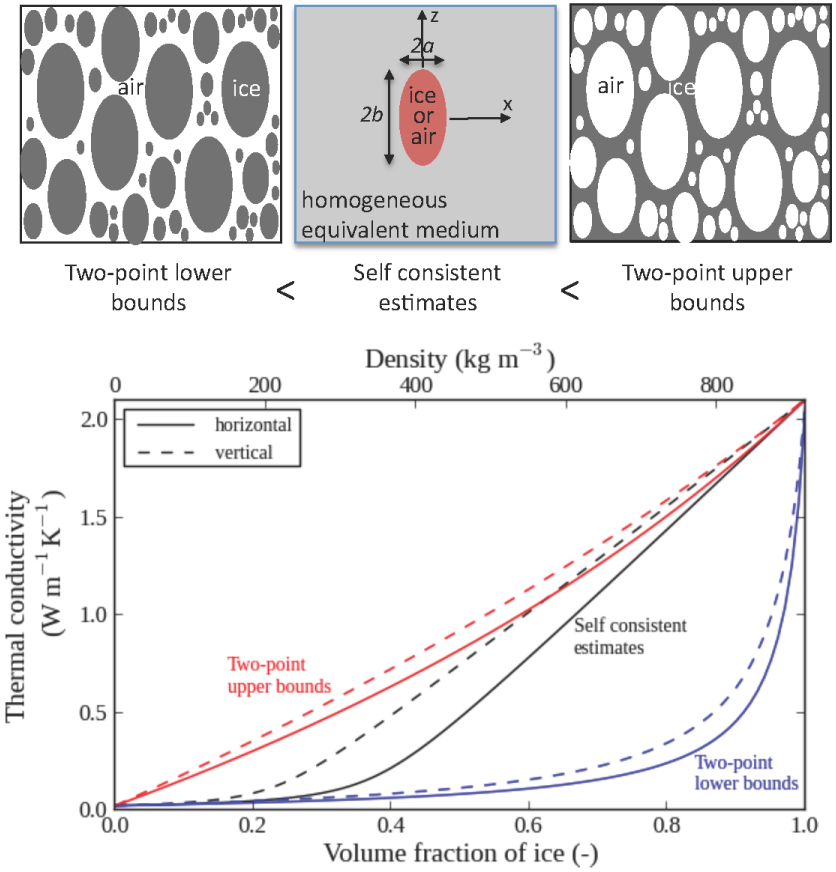

Fig. 3. Schematic representation of the microstructure corresponding to the two-point bounds and the self consistent scheme. Effective thermal conductivity versus ice volume fraction when b/a = 1.45: self consistent estimates (black curves), two-points lower (blue curves) and upper (red curves) bounds.

TCD
8, 1407–1451, 2014

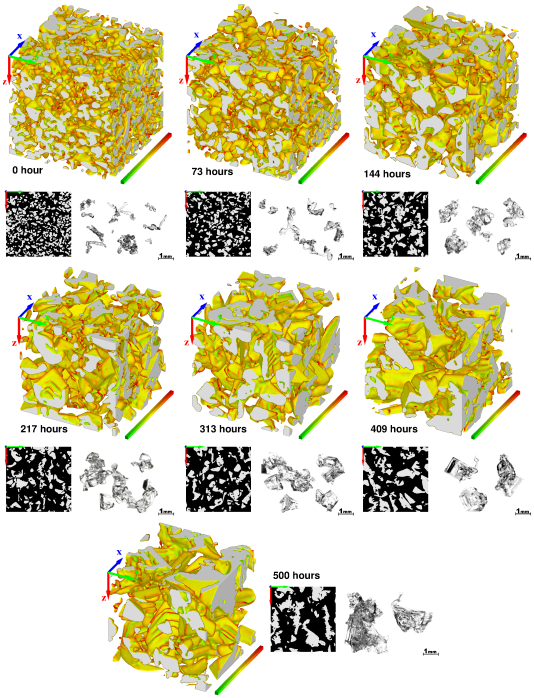

Fig. 4. Microstructure evolution during the experiment of TG metamorphism. For each stage of the evolution, the following views are given: (i) 3-D images of the snow samples where colors represent the mean curvature of the surfaces, ranging from −36 to +36 mm^{-1}. Convexities, flat shapes and concavities are shown in red, yellow and green, respectively. Images have a size of 3 mm × 3 mm × 3 mm. For a better visualization of the facetted shapes, the images are presented "upside down". The arrows in blue, green and red correspond to the x, y and z directions of the images, respectively. (ii) Vertical cross-sections from 3-D images of 5.5 mm × 5.5 mm × 5.5 mm, where ice is in white and air in black. (iii) Photographs of snow grains corresponding to the 3-D images.

TCD
8, 1407–1451, 2014

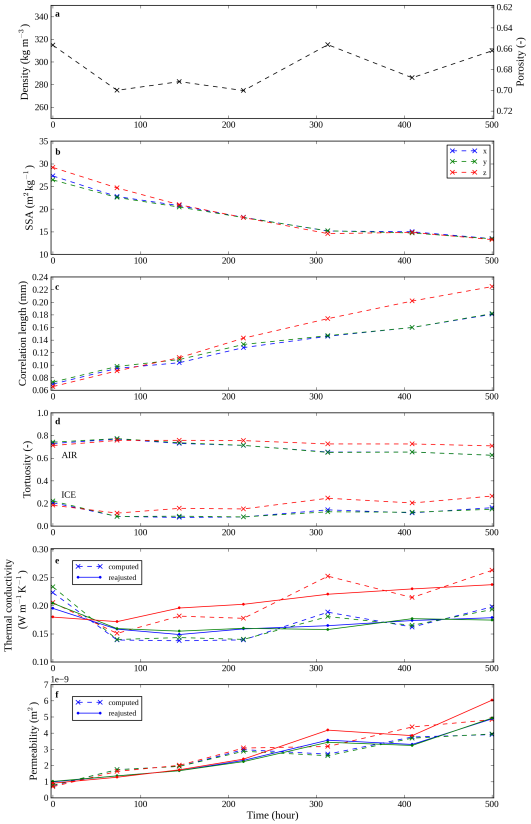

Fig. 5. Time evolution of microstructural and physical properties of snow during the whole temperature gradient experiment. Values in the x, y and z directions are given in blue, green and red, respectively.

TCD
8, 1407–1451, 2014

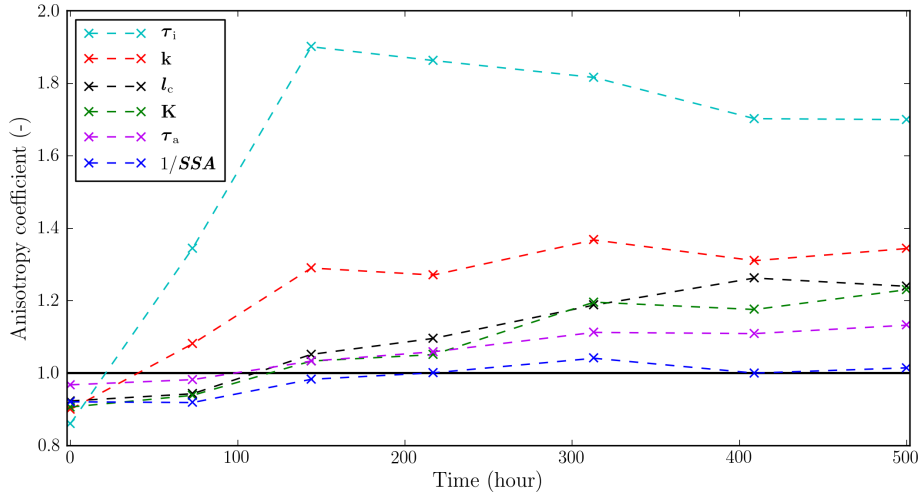

Fig. 6. Time evolution of the anisotropy coefficient of the whole computed properties.

TCD
8, 1407–1451, 2014

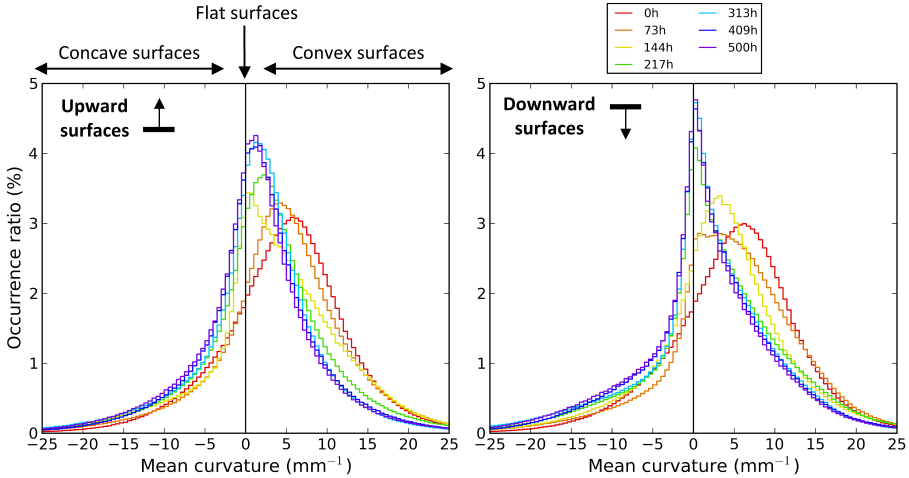

Fig. 7. Time evolution of the mean curvature distribution computed from the upward (left) and downward (right) surfaces of the 3-D images.

TCD
8, 1407–1451, 2014

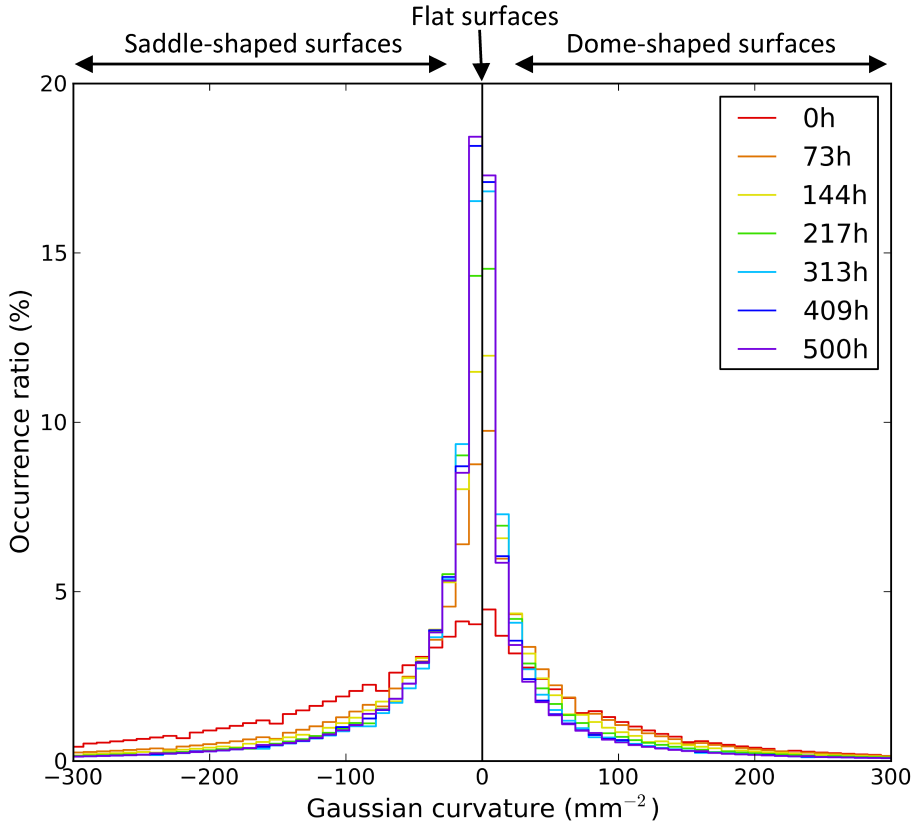

Fig. 8. Time evolution of the Gaussian curvature distribution computed from the whole surface of the 3-D images.

TCD
8, 1407–1451, 2014

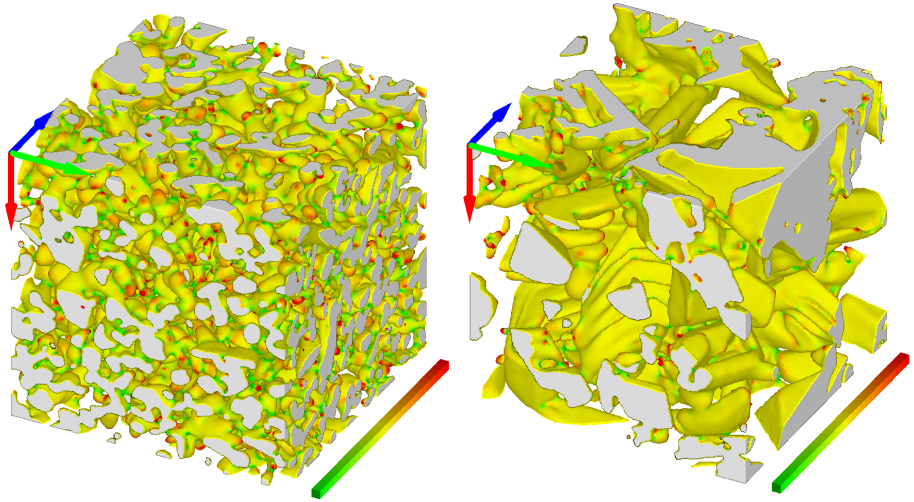

Fig. 9. The initial (left) and final (right) 3-D images of the experiment where colors represent the Gaussian curvature of the surfaces, ranging from −781 to +781 mm^{-2}. Dome-shaped (concave or convex), flat or cylindrical and saddle-shaped surfaces are shown in red, yellow and green, respectively. Images have a size of 3 mm × 3 mm × 3 mm. For a better visualization of the facetted shapes, the images are presented "upside down". The arrows in blue, green and red correspond to the *x*, *y* and *z* directions of images, respectively.

TCD
8, 1407–1451, 2014

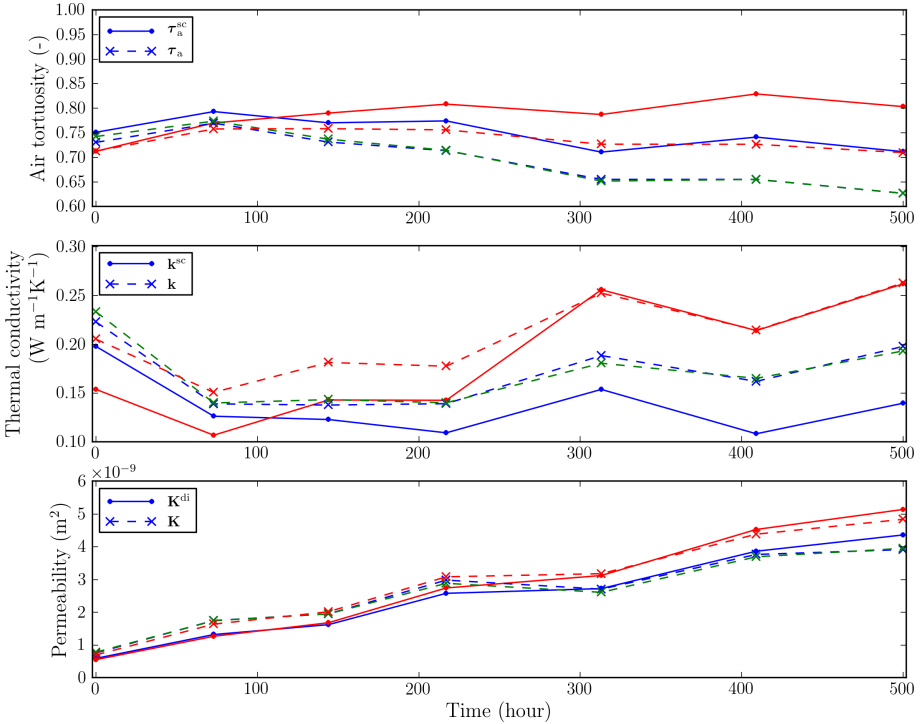

Fig. 10. Time evolution of air tortuosity, thermal conductivity and permeability during the whole experiment. Comparison between values computed from 3-D images in the x, y and z directions (dashed lines in blue, green and red, respectively) and values given by analytical models in the xy and z directions (solid lines in blue and red, respectively).

TCD
8, 1407–1451, 2014

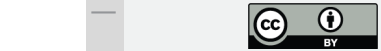

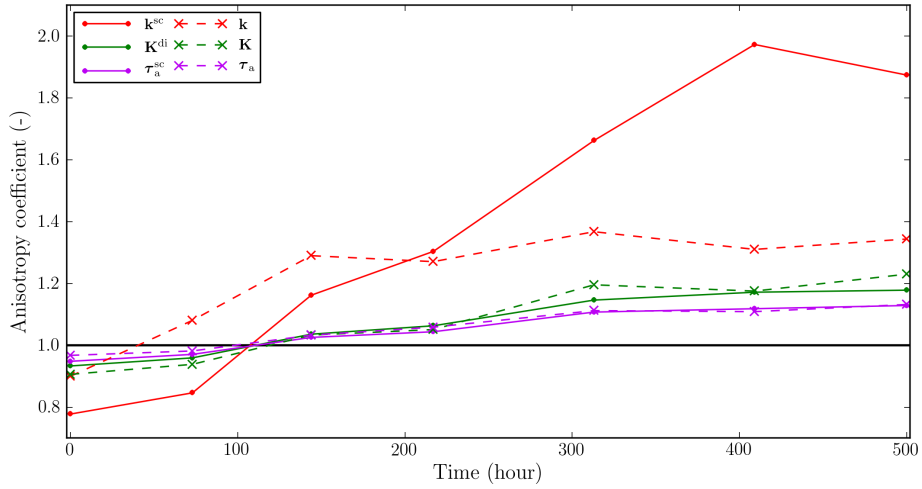

Fig. 11. Time evolution of the anisotropy coefficients of air tortuosity, thermal conductivity and permeability. Comparison between coefficients deduced from values computed on 3-D images (dashed lines) and values given by analytical models (solid lines).

TCD
8, 1407–1451, 2014